Vol 459|28 May 2009|doi:10.1038/nature08005

LETTERS

Synthesizing arbitrary quantum states in a superconducting resonator

Max Hofheinz[1], H. Wang[1], M. Ansmann[1], Radoslaw C. Bialczak[1], Erik Lucero[1], M. Neeley[1], A. D. O'Connell[1], D. Sank[1], J. Wenner[1], John M. Martinis[1] & A. N. Cleland[1]

The superposition principle is a fundamental tenet of quantum mechanics. It allows a quantum system to be 'in two places at the same time', because the quantum state of a physical system can simultaneously include measurably different physical states. The preparation and use of such superposed states forms the basis of quantum computation and simulation[1]. The creation of complex superpositions in harmonic systems (such as the motional state of trapped ions[2], microwave resonators[3–5] or optical cavities[6]) has presented a significant challenge because it cannot be achieved with classical control signals. Here we demonstrate the preparation and measurement of arbitrary quantum states in an electromagnetic resonator, superposing states with different numbers of photons in a completely controlled and deterministic manner. We synthesize the states using a superconducting phase qubit to phase-coherently pump photons into the resonator, making use of an algorithm[7] that generalizes a previously demonstrated method of generating photon number (Fock) states in a resonator[8]. We completely characterize the resonator quantum state using Wigner tomography, which is equivalent to measuring the resonator's full density matrix.

The quantum state of a resonator is extraordinarily rich, with infinitely many energy levels, of which each can have a non-zero amplitude. However, this richness is difficult to access when driving a resonator with a classical signal, as the two adjustable parameters of an on-resonant drive, the amplitude and the phase, give very limited control. Creating an arbitrary quantum state instead requires a nonlinear element and a control scheme with many parameters. Here we demonstrate quantum state generation in a resonator by interposing a highly nonlinear Josephson phase qubit[9] between a superconducting resonator and a classical signal. A qubit[4,5,10–14] has two quantum degrees of freedom, the relative amplitude and phase of its ground $|g\rangle$ and excited $|e\rangle$ energy eigenstates. This simplicity allows full quantum control of a qubit with a classical signal[15]. By following a sequence of steps developed for trapped ions[2,7] (and later adapted to charge qubits[16]), where each step involves creating a particular qubit state and then having the qubit interact with the resonator for a controlled time, we synthesize arbitrary states in the resonator. The preparation is deterministic, unlike methods involving probabilistic projective measurements[17]. After the preparation, we analyse the resonator state using Wigner tomography[18–22], mapping out the Wigner quasi-probability distribution[23,24], from which we extract the resonator's full density matrix.

The quantum circuit we used is shown in Fig. 1a. The phase qubit is capacitively coupled to a superconducting coplanar waveguide resonator, and the circuit includes control lines for the qubit and resonator, and a qubit measurement circuit described elsewhere[25]. This circuit is similar to that used previously to generate Fock states in a resonator[8]; here, however, most of the superconducting wiring is made of rhenium in place of aluminium, and we removed unnecessary dielectric, reducing dissipative elements in the circuit.

The qubit frequency $\omega_q/2\pi$ can be externally adjusted, whereas the resonator frequency $\omega_r/2\pi = 6.570$ GHz is fixed. This allows us to

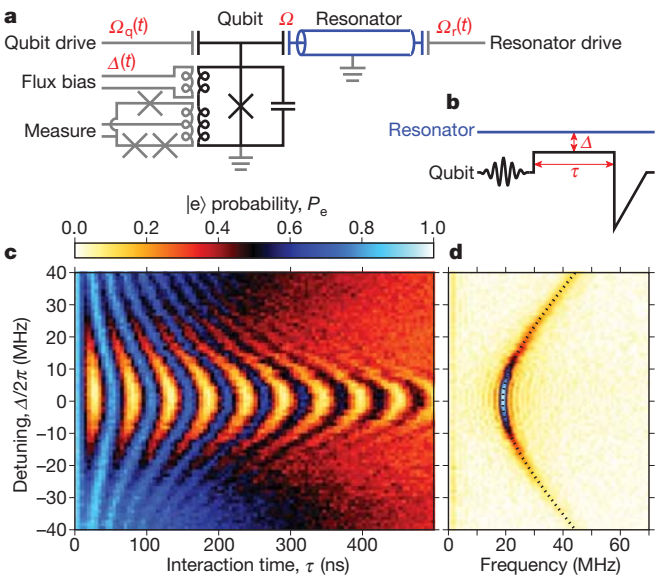

Figure 1 | Circuit diagram and one photon Rabi-swap oscillations between qubit and resonator. a, The qubit (black) is made from a Josephson junction (cross) and a capacitor, biased through a shunting inductor. The qubit detuning Δ is adjusted through a flux bias coil, and the qubit state is read out by a three-Josephson-junction superconducting quantum interference device (SQUID). The coplanar waveguide resonator (blue) has fixed capacitive coupling Ω to the qubit, and small capacitors couple external microwave signals Ω_q and Ω_r to the qubit and resonator. The device was measured in a dilution refrigerator at 25 mK. The qubit relaxation and dephasing times were respectively $T_{1,q} \approx 650$ ns and $T_{2,q} \approx 150$ ns, and the resonator relaxation time was $T_{1,r} \approx 3.5$ μs with no measurable dephasing. **b**, Schematic of Rabi-swap pulse sequence. The qubit starts in its ground state, detuned at its typical off-resonance point by $\Delta_{off}/2\pi = -463\,\text{MHz} \approx -25\Omega/2\pi$ from the resonator. A resonant qubit microwave π-pulse brings the qubit to its excited state $|e\rangle$, injecting one quantum of energy into the system. A flux bias pulse reduces the qubit detuning Δ from the resonator for a controlled time τ, and the qubit state is then measured with a current pulse. **c**, Excited state probability P_e versus detuning Δ and interaction time τ. P_e is obtained by averaging 600 repetitions. **d**, Fourier transform of data in **c**, showing the expected hyperbolic relation between detuning Δ and swap frequency $\sqrt{\Omega^2+\Delta^2}/2\pi$ (dotted line), and the expected fall-off in probability (colour scale). Resonance $\Delta = 0$ corresponds to lowest swap frequency and maximum probability amplitude.

[1]Department of Physics, University of California, Santa Barbara, California 93106, USA.

Table 1 | Sequence to generate the resonator state $|\psi\rangle = |1\rangle + i|3\rangle$

Sequence of states, operations	Operational parameter	System state, parameter value
$\|\psi\rangle$		$\|g\rangle(0.707\|1\rangle+0.707i\|3\rangle)$
S_3	$\tau_3\Omega$	1.81
Q_3	q_3	3.14
$\|\psi_2\rangle$		$\|g\rangle(-0.557i\|0\rangle+0.707\|2\rangle)+0.436\|e\rangle\|1\rangle$
Z_2	$t_2\Delta$	4.71
S_2	$\tau_2\Omega$	1.44
Q_2	q_2	$-2.09 - 2.34i$
$\|\psi_1\rangle$		$(0.553-0.62i)\|g\rangle\|1\rangle-(0.371+0.416i)\|e\rangle\|0\rangle$
Z_1	$t_1\Delta$	3.26
S_1	$\tau_1\Omega$	1.96
Q_1	q_1	$-2.71-1.59i$
$\|\psi_0\rangle$		$(0.197-0.98i)\|g\rangle\|0\rangle$

This resonator state is used for the measurements described in Fig. 2. The sequence is computed top to bottom, but applied bottom to top. The area and phase for the nth qubit drive Q_n is $q_n = \int \Omega_q(t)e^{i\Delta_{off}t}dt$ ($t = 0$ being the time when the qubit is tuned into resonance directly after the step Q_n), the time on-resonance for the qubit–resonator swap operation S_n is τ_n, and the time off-resonance (mod $2\pi/\Delta$) for the phase rotation Z_n is t_n. We note that the initial state $|\psi_0\rangle$ differs by an overall phase factor from the ground state $|g\rangle|0\rangle$, but this is not detectable. State descriptions are shown bold; operations are not in bold.

describe the system with a Hamiltonian in the resonator rotating frame, so that the resonator states have zero frequency:

$$\frac{H}{\hbar} = \Delta(t)\sigma_+\sigma_- + \left(\frac{\Omega}{2}\sigma_+ a + \frac{\Omega_q(t)}{2}\sigma_+ + \frac{\Omega_r(t)}{2}a^\dagger\right) + \text{h.c.} \quad (1)$$

Here σ_+ and σ_- ($a^\dagger$ and a) are the qubit (resonator) raising and lowering operators, and h.c. is the Hermitian conjugate of the terms in parentheses. The first term is the qubit energy, which appears as the qubit–resonator detuning $\Delta(t) = \omega_q(t) - \omega_r$. The first term in the parentheses gives the qubit–resonator interaction, proportional to the fixed interaction strength $\Omega/2\pi = 19$ MHz, while the second and third terms give the effect of the external microwave drive signals applied to the qubit and resonator; these parameters $\Omega_q(t)$ and $\Omega_r(t)$ are complex to account for amplitude and phase. All control signals in equation (1) vary on a ~2 ns timescale, long compared to $2\pi/\omega_r$, so counter-rotating terms in equation (1) are neglected.

Although the coupling Ω is fixed, we control the qubit–resonator interaction by adjusting the qubit frequency between two operating points, one with qubit and resonator exactly on resonance ($\Delta_{on} = 0$), the other with the qubit well off-resonance ($|\Delta_{off}| \gg \Omega$). On resonance, the coupling will produce an oscillation where a single photon transfers between qubit and resonator with unit probability, alternating between states with, say, the qubit in its ground state with n photons in the resonator, $|g\rangle \otimes |n\rangle = |g, n\rangle$, and the qubit in its excited state with $n-1$ photons in the resonator, $|e, n-1\rangle$; this occurs at the n-photon 'Rabi-swap' frequency $\sqrt{n}\Omega$. Off resonance, the system oscillates at a higher frequency $\sqrt{n\Omega^2+\Delta^2}$ but with reduced $|e, n-1\rangle$ probability $n\Omega^2/(n\Omega^2+\Delta^2) < 1$. This detuning dependence is shown in Fig. 1 for $n = 1$ photon and small detunings $|\Delta| \lesssim \Omega$. At our typical off-resonance operating point $\Delta_{off} \approx -25\Omega$, the photon transfer probability is only 0.0016 n, so the coupling is essentially turned off.

We determine from Fig. 1 the flux bias for on-resonance tuning ($\Delta = 0$) and the one-photon swap time. Using these parameters, we can pump photons one at a time into the resonator by repeatedly exciting the detuned qubit from $|g\rangle$ to $|e\rangle$ using a qubit microwave π-pulse, followed by a controlled-time, on-resonance photon swap[8], where we scale the swap time for the nth photon by $1/\sqrt{n}$. Precise scaling of this swap time is crucial for proper control, and was verified for up to 15 photons (see Supplementary Information).

Our goal is to synthesize arbitrary N-photon states in the resonator with the qubit in its ground state, disentangled from the resonator. Our target state for the coupled system is

$$|\psi\rangle = |g\rangle \otimes \sum_{n=0}^{N} c_n|n\rangle \quad (2)$$

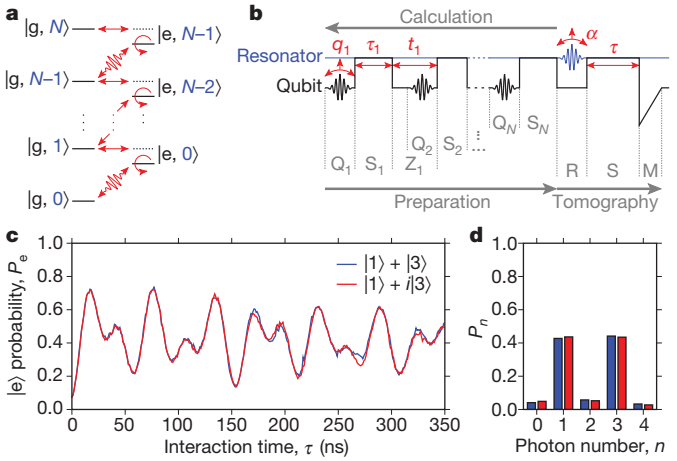

Figure 2 | Sequence to synthesize an arbitrary resonator state. **a**, Qubit–resonator energy ladder. Levels are depicted by dotted and solid lines when tuned ($\Delta = 0$) and detuned, respectively; qubit states are in black, resonator states are in blue. Three types of operations (in red) are used in state preparation: qubit drive operations Q_n, indicated by undulating lines; qubit–resonator swap operations S_n, indicated by straight horizontal lines; and phase rotations of the qubit state Z_n, indicated by circles. Each operation affects all the levels in the diagram. **b**, Microwave pulse sequence. The qubit and resonator are traced in black and blue, respectively, with qubit operations in red. The sequence is computed in reverse order by emptying energy levels from top to bottom. To descend the first step of the ladder in **a**, a swap operation S_N transfers the highest occupied resonator state to the qubit, $|g, N\rangle \rightarrow |e, N-1\rangle$. This operation also performs incomplete transfers on all the lower-lying states, as do the succeeding steps. A qubit microwave drive Q_N then transfers all the population of $|e, N-1\rangle$ to $|g, N-1\rangle$ (in general this step is not a π-pulse as $|g, N-1\rangle$ is not completely emptied by pulse S_N). For the second step down the ladder, a rotation Z_{N-1} first adjusts the phase of the qubit excited state $|e\rangle$ relative to the ground state $|g\rangle$. The succeeding swap pulse S_{N-1} can then move the entire population of $|g, N-1\rangle$ to $|e, N-2\rangle$. This sequence is repeated N times until the ground state $|g, 0\rangle$ is reached. Steps Q_n are performed with resonant qubit microwave pulses of amplitude q_n, swaps S_n achieved by bringing the qubit and resonator on resonance for time τ_n, and phase rotations Z_n completed by adjusting the detuning time t_n; see Table 1 for a detailed example. After state preparation, tomographic readout is performed: a displacement $D(-\alpha)$ of the resonator is performed by a microwave pulse R to the resonator, then the resonator state is probed by a qubit–resonator swap S for a variable interaction time τ, and finally the qubit state measured by the measurement pulse M. **c**, Plot of the qubit excited state probability P_e versus interaction time τ for the resonator states $|\psi_a\rangle = |1\rangle + |3\rangle$ (blue) and $|\psi_b\rangle = |1\rangle + i|3\rangle$ (red), taken with $\alpha = 0$. We clearly observe oscillations at the $|1\rangle$ and $|3\rangle$ Fock state frequencies. Nearly identical traces for $|\psi_a\rangle$ and $|\psi_b\rangle$ indicate the same photon number probability distribution, as expected. **d**, Photon number distributions for $|\psi_a\rangle$ (blue) and $|\psi_b\rangle$ (red). Both states are equal superpositions of $|1\rangle$ and $|3\rangle$ but the phase information that distinguishes the two states is lost.

with complex amplitude c_n for the nth Fock state. Law and Eberly[7] showed that these states can be generated by sequentially exciting the qubit into the proper superposition of $|g\rangle$ and $|e\rangle$, and then performing a partial transfer to the resonator. As illustrated in Fig. 2, and detailed in Table 1, a sequence generating the desired state can be found by solving the time-reversed problem: starting with the desired final state, we first transfer the amplitude of the highest occupied resonator Fock state to the qubit, then remove the excitation from the subsequently detuned qubit using a classical microwave signal, and repeat until the ground state $|g, 0\rangle$ is reached. The actual control signals are sequenced in the normal (un-reversed) order to generate the desired final state from the initial ground state. We note that the Law and Eberly protocol[7] assumes an adjustable phase for the qubit–resonator coupling Ω, which equation (1) does not allow; instead, we correct the relative phases of $|g, n\rangle$ and $|e, n-1\rangle$ by adjusting the time t_n over which the qubit and resonator are detuned.

To calibrate the actual microwave signals needed to implement this sequence, it is impractical to individually tune each sequence step,

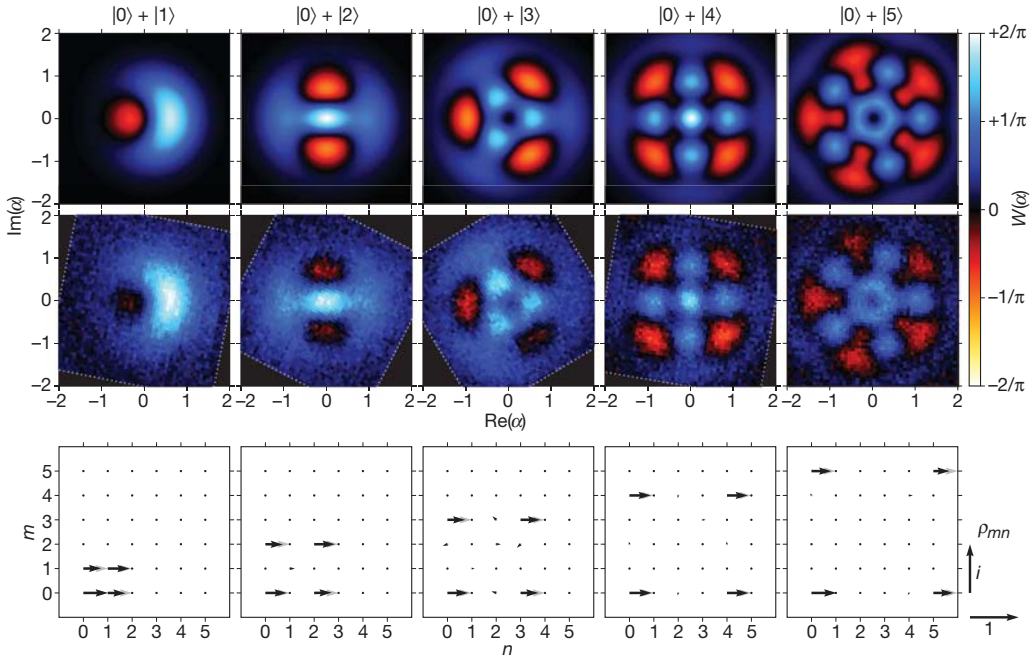

Figure 3 | Wigner tomography of superpositions of resonator Fock states $|0\rangle + |N\rangle$. The top row displays the theoretical form of the Wigner function $W(\alpha)$ as a function of the complex resonator amplitude α in photon number units, for states $N = 1$ to 5. The measured Wigner functions are shown in the middle row, with the colour scale bar on the far right. Negative quasi-probabilities are clearly measured. The experimental Wigner functions have been rotated to match theory, compensating for a phase delay between the qubit and resonator microwave lines; the measured area is bounded by a dotted white line. The bottom row displays the calculated (grey) and measured (black) values for the resonator density matrix ρ, projected onto the number states $\rho_{mn} = \langle m|\rho|n\rangle$. The magnitude and phase of ρ_{mn} is represented by the length and direction of an arrow in the complex plane (for scale, see key on right). The fidelities $F = \sqrt{\langle\psi|\rho|\psi\rangle}$ between the desired states $|\psi\rangle$ and the measured density matrices ρ are, from left to right, $F = 0.92$, 0.89, 0.88, 0.94 and 0.91. Each of the 51 by 51 pixels (61 by 61 for $N = 5$) in the Wigner function represents a local measurement. The value of $W(\alpha)$ is calculated at each pixel from 50 (41 for $N = 4$ and 5) interaction times τ, each repeated 900 times to give $P_e(\tau)$. This direct mapping of the Wigner function takes $\sim 10^8$ measurements or ~ 5 h.

because the intermediate states are quite complex and measuring them is time-consuming. Instead we perform careful calibrations of the experimental system independent of the particular state preparation (see Supplementary Information).

An initial check of the outcome of the preparation is to determine if the qubit ends up in the ground state $|g\rangle$, as desired. We find that this holds with a probability typically greater than 80%, the remaining 20% being compatible with decoherence during the preparation sequence (see Supplementary Information).

With the qubit near its ground state and not entangled with the resonator, we can use the qubit to measure the resonator state. By bringing the qubit and resonator into resonance for a variable time τ and subsequently measuring the probability P_e for the qubit excited state, we can determine[8] the n-photon probabilities $P_n = |c_n|^2$, correcting for measurement fidelity and initial qubit state probability (see Supplementary Information). In Fig. 2c we compare $P_e(\tau)$ for the experimentally prepared states $|\psi_a\rangle = |1\rangle + |3\rangle$ and $|\psi_b\rangle = |1\rangle + i|3\rangle$, showing the expected superposed oscillations corresponding to the $|1\rangle$ and $|3\rangle$ Fock states. This measurement however only yields the probabilities P_n: the relative phases of the Fock states are lost, so the states $|\psi_a\rangle$ and $|\psi_b\rangle$ cannot be distinguished.

To measure the complex amplitudes c_n, we need to probe the interference between the superposed Fock states. This may be done using Wigner tomography[19,21,24], which maps out the Wigner quasi-probability distribution $W(\alpha)$ as a function of the phase space amplitude α of the resonator (see Supplementary Information). Wigner tomography is performed by following the functional definition:

$$W(\alpha) = \frac{2}{\pi}\langle\psi|D^{\dagger}(-\alpha)\Pi\, D(-\alpha)|\psi\rangle \qquad (3)$$

The resonator state $|\psi\rangle$ is first displaced by the operator $D(-\alpha)$, implemented with a microwave drive pulse $-\alpha = (1/2)\int \Omega_r(t)\mathrm{d}t$. The photon number probabilities P_n are then measured and finally the parity $\langle\Pi\rangle = \sum_n (-1)^n P_n$ evaluated. The corresponding pulse sequence is depicted in Fig. 2b.

Calculated and measured Wigner functions are shown in Fig. 3 top and middle rows, respectively, for the resonator states $|0\rangle + |N\rangle$, with $N = 1$ to 5. The structures of the Wigner functions match well, including fine details, indicating that the superposed states are created and measured accurately. The density matrices for each state are also calculated (Fig. 3 bottom row; see Supplementary Information) and are as expected. The Wigner function of non-classical states has been measured previously, either calculated via an inverse Radon transform[18,26,27], or measured at enough points to fit the density matrix[3,28], from which the Wigner function is reconstructed. The high resolution direct mapping of the Wigner function used here is an important verification of our state preparation. The good agreement in shape shows that very pure superpositions of $|0\rangle$ and $|N\rangle$ have been created. Slight deviations in amplitude can be due to small errors in the read-out process, the relative amplitudes of the $|0\rangle$ and $|N\rangle$ states, or statistical mixtures with other Fock states.

The data in Fig. 3 do not demonstrate phase control between Fock states, as a change in the relative phase of a two-state superposition only rotates the Wigner function. The phase accuracy may be robustly demonstrated by preparing states with a superposition of three Fock states, as changing the phase of one state then changes the shape of the Wigner function. Figure 4 shows Wigner tomography for a superposition of the $|0\rangle$, $|3\rangle$ and $|6\rangle$ Fock states, where the phase of the $|3\rangle$ state has been changed in each of the five panels. The shape of the calculated and measured Wigner functions (Fig. 4 top and middle rows, respectively) again agree, including small details, indicating that precise phase control has been achieved. The calculated and measured density matrices (Fig. 4 bottom row) also match well.

In conclusion, we have generated and measured arbitrary superpositions of resonator quantum states. State preparation is deterministic and 'on-demand', requiring no projective measurements, and limited

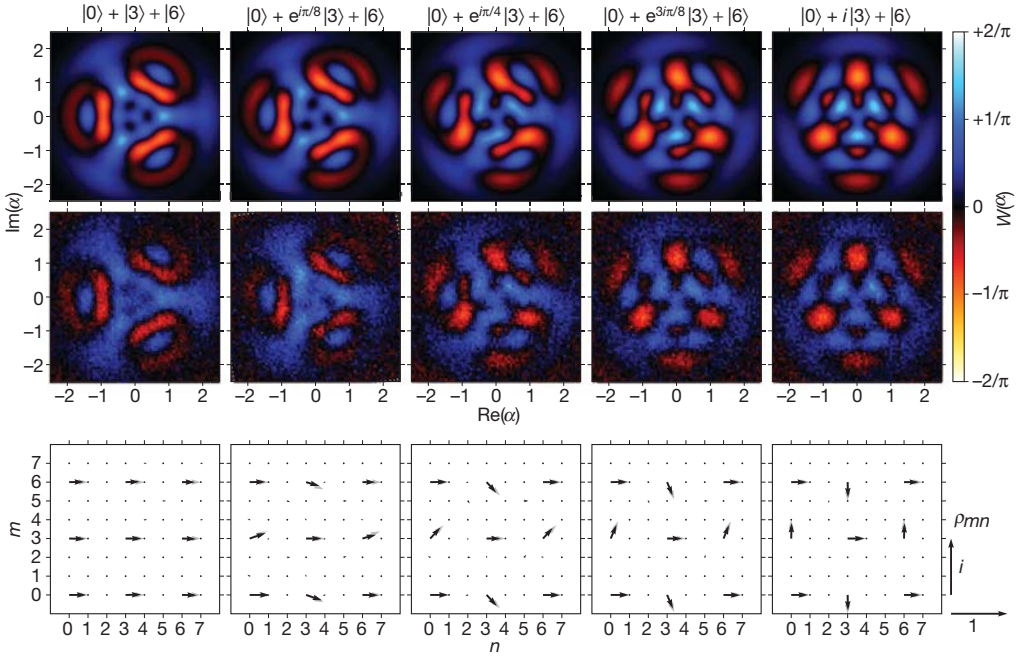

Figure 4 | Wigner tomography of the states $|0\rangle + e^{ik\pi/8}|3\rangle + |6\rangle$ for five values of phase $k = 0$ to 4. The top row is calculated, whereas the middle row shows measurements. The bottom row displays the calculated (grey) and measured (black) values for the density matrix obtained from the Wigner functions, displayed as for Fig. 3. The fidelities between the expected states and the measured density matrices are, from left to right, $F = 0.89$, 0.91, 0.91, 0.91 and 0.91.

to about ten photons, mainly by decoherence[29]. The accuracy of the prepared states demonstrates that a qubit, when controlled with high fidelity, is ideally suited for synthesizing and measuring arbitrary quantum states of light.

Received 15 January; accepted 19 March 2009.

1. Nielsen, M. A. & Chuang, I. L. *Quantum Computation and Quantum Information* (Cambridge Univ. Press, 2000).
2. Ben-Kish, A. *et al.* Experimental demonstration of a technique to generate arbitrary quantum superposition states of a harmonically bound spin-1/2 particle. *Phys. Rev. Lett.* **90,** 037902 (2003).
3. Deléglise, S. *et al.* Reconstruction of non-classical cavity field states with snapshots of their decoherence. *Nature* **455,** 510–514 (2008).
4. Houck, A. A. *et al.* Generating single microwave photons in a circuit. *Nature* **449,** 328–331 (2007).
5. Sillanpää, M. A., Park, J. I. & Simmonds, R. W. Coherent quantum state storage and transfer between two phase qubits via a resonant cavity. *Nature* **449,** 438–442 (2007).
6. Boozer, A. D., Boca, A., Miller, R., Northup, T. E. & Kimble, H. J. Reversible state transfer between light and a single trapped atom. *Phys. Rev. Lett.* **98,** 193601 (2007).
7. Law, C. K. & Eberly, J. H. Arbitrary control of a quantum electromagnetic field. *Phys. Rev. Lett.* **76,** 1055–1058 (1996).
8. Hofheinz, M. *et al.* Generation of Fock states in a superconducting quantum circuit. *Nature* **454,** 310–314 (2008).
9. Martinis, J. M., Devoret, M. H. & Clarke, J. Energy-level quantization in the zero-voltage state of a current-biased Josephson junction. *Phys. Rev. Lett.* **55,** 1543–1546 (1985).
10. Clarke, J. & Wilhelm, F. K. Superconducting quantum bits. *Nature* **453,** 1031–1042 (2008).
11. Vion, D. *et al.* Manipulating the quantum state of an electrical circuit. *Science* **296,** 886–889 (2002).
12. Niskanen, A. O. *et al.* Quantum coherent tunable coupling of superconducting qubits. *Science* **316,** 723–726 (2007).
13. Plantenberg, J. H., de Groot, P. C., Harmans, C. J. P. M. & Mooij, J. E. Demonstration of controlled-NOT quantum gates on a pair of superconducting quantum bits. *Nature* **447,** 836–839 (2007).
14. Fink, J. M. *et al.* Climbing the Jaynes-Cummings ladder and observing its $\sqrt{n}$ nonlinearity in a cavity QED system. *Nature* **454,** 315–318 (2008).
15. Steffen, M. *et al.* State tomography of capacitively shunted phase qubits with high fidelity. *Phys. Rev. Lett.* **97,** 050502 (2006).
16. Liu, Y. X. *et al.* Generation of non-classical photon states using a superconducting qubit in a quantum electrodynamic microcavity. *Europhys. Lett.* **67,** 941–947 (2004).
17. Vogel, K., Akulin, V. M. & Schleich, W. P. Quantum state engineering of the radiation field. *Phys. Rev. Lett.* **71,** 1816–1819 (1993).
18. Smithey, D. T., Beck, M., Raymer, M. G. & Faridani, A. Measurement of the Wigner distribution and the density matrix of a light mode using optical homodyne tomography: Application to squeezed states and the vacuum. *Phys. Rev. Lett.* **70,** 1244–1247 (1993).
19. Banaszek, K. & Wódkiewicz, K. Direct probing of quantum phase space by photon counting. *Phys. Rev. Lett.* **76,** 4344–4347 (1996).
20. Lutterbach, L. G. & Davidovich, L. Method for direct measurement of the Wigner function in cavity QED and ion traps. *Phys. Rev. Lett.* **78,** 2547–2550 (1997).
21. Banaszek, K., Radzewicz, C., Wódkiewicz, K. & Krasiński, J. S. Direct measurement of the Wigner function by photon counting. *Phys. Rev. A* **60,** 674–677 (1999).
22. Bertet, P. *et al.* Direct measurement of the Wigner function of a one-photon Fock state in a cavity. *Phys. Rev. Lett.* **89,** 200402 (2002).
23. Wigner, E. On the quantum correction for thermodynamic equilibrium. *Phys. Rev.* **40,** 749–759 (1932).
24. Haroche, S. & Raimond, J.-M. *Exploring the Quantum — Atoms, Cavities and Photons* (Oxford Univ. Press, 2006).
25. Neeley, M. *et al.* Transformed dissipation in superconducting quantum circuits. *Phys. Rev. B* **77,** 180508 (2008).
26. Breitenbach, G., Schiller, S. & Mlynek, J. Measurement of the quantum states of squeezed light. *Nature* **387,** 471–475 (1997).
27. Lvovsky, A. I. & Babichev, S. A. Synthesis and tomographic characterization of the displaced Fock state of light. *Phys. Rev. A* **66,** 011801 (2002).
28. Leibfried, D. *et al.* Experimental determination of the motional quantum state of a trapped atom. *Phys. Rev. Lett.* **77,** 4281–4285 (1996).
29. Wang, H. *et al.* Measurement of the decay of Fock states in a superconducting quantum circuit. *Phys. Rev. Lett.* **101,** 240401 (2008).

Supplementary Information is linked to the online version of the paper at www.nature.com/nature.

Acknowledgements Devices were made at the UCSB Nanofabrication Facility, a part of the NSF-funded National Nanotechnology Infrastructure Network. We thank M. Geller for discussions. This work was supported by IARPA (grant W911NF-04-1-0204) and by the NSF (grant CCF-0507227).

Author Contributions M.H. performed the experiments and analysed the data. H.W. improved the resonator design and fabricated the sample. J.M.M. and E.L. designed the custom electronics and M.H. developed the calibrations for it. M.A. and M.N. provided software infrastructure. All authors contributed to the fabrication process, qubit design or experimental set-up. M.H., J.M.M. and A.N.C. conceived the experiment and co-wrote the paper.

Author Information Reprints and permissions information is available at www.nature.com/reprints. Correspondence and requests for materials should be addressed to A.N.C. (Cleland@physics.ucsb.edu).

doi: 10.1038/nature08005

Supplementary Information

1. VOODOO CAT STATE

In the main article we display the measured and calculated Wigner functions for the resonator states $|0\rangle + |N\rangle$ and for the states $|1\rangle + \exp(ik\pi/8)|3\rangle + |6\rangle$, $k = 0$ to 4. In Fig. S1 we display the "Voodoo cat" state, which involves Fock states as high as $|9\rangle$, fully demonstrating the range of states we can currently prepare.

2. WIGNER TOMOGRAPHY AND DENSITY MATRIX

The Wigner function $W(\alpha)$ and density matrix ρ are related via the trace

$$W(\alpha) = \frac{2}{\pi}\mathrm{Tr}\left(D(-\alpha)\rho D(\alpha)\,\Pi\right). \tag{4}$$

To measure the Wigner function, we first prepare the resonator state, as given by the density matrix ρ. During state analysis, microwaves drive the resonator and coherently displace the resonator state by $-\alpha = (1/2)\int \Omega_\mathrm{r}(t)\mathrm{d}t$, as described by the operator $D(-\alpha) = D^\dagger(\alpha) = \exp(\alpha^* a - \alpha a^\dagger)$. For the displaced resonator state $\rho' = D(-\alpha)\rho D(\alpha)$, we determine the diagonal elements ρ'_{nn} by measuring $P_\mathrm{e}(\tau)$ during a swap interaction[8] (see below). As the Fock states are eigenstates of the parity operator Π with eigenvalues 1 (-1) for even (odd) Fock states, the Wigner function can simply be calculated as

$$W(\alpha) = (2/\pi)\sum_n (-1)^n \rho'_{nn}(-\alpha). \tag{5}$$

We note that the Wigner function can also be calculated directly from the time trace $P_\mathrm{e}(\tau)$ via a Fresnel transform[30], requiring only a short time scan, but yielding slightly less precise results in our case. The parity can also be measured directly in the dispersive limit[24], obviating the time scan, but the dispersive regime is incompatible with the parameters we need for state preparation.

The amplitude scale and the phase of the microwave pulse α are calibrated by a best fit between the measured and calculated Wigner distributions. Small variations ($\sim 5\,\%$) in the scale calibration were found for the various states measured here, including the coherent state, and thus an average was used. The magnitude of the scale factor is in good agreement with the attenuation of the microwave line and its coupling capacitor.

The density matrix can be calculated from the Wigner function by inverting Eq. (4). However, to make full use of the measured data, we instead calculate the density matrix ρ directly from the full set of measured photon number probabilities[28] by solving the set of linear equations

$$\rho'_{nn}(\alpha_m) = \langle n|D(-\alpha_m)\rho D(\alpha_m)|n\rangle = \sum_{j,i} M_{nmji}\rho_{ji}, \tag{6}$$

one for each extracted photon number n and one for each measured displacement α_m. The matrix

$$M_{nmji} = \langle j|D(\alpha_m)|n\rangle^* \langle i|D(\alpha_m)|n\rangle\ , \tag{7}$$

is calculated by expanding the displacement operator $D(\alpha) = \exp(\alpha a^\dagger - \alpha^* a)$ in the Fock basis:

$$\langle p|D(\alpha)|q\rangle = e^{-|\alpha|^2/2}\sqrt{p!q!}\sum_{k=0}^{\min\{p,q\}} \frac{\alpha^{(p-k)}(-\alpha^*)^{(q-k)}}{k!(p-k)!(q-k)!}\ . \tag{8}$$

We solve the largely overdetermined linear system of Eq. (6) by least-squares while restricting ρ to be hermitian. Due to noise, ρ can have small negative eigenvalues. Therefore we diagonalise ρ, set the unphysical negative eigenvalues to zero, and then transform back to the Fock basis. Finally we normalise ρ.

3. PHOTON NUMBER READOUT

At the end of the state preparation sequence for the resonator, the qubit is ideally in its ground state. We verify this by performing state tomography of the qubit[15], yielding a qubit density matrix that is very close to the ground state. Typically, the off-diagonal elements of the density matrix are very small, but the excited state probability is not zero, corresponding to a Bloch vector pointing close to the $|\mathrm{g}\rangle$ state: For the state generation shown in Fig. 4, the angle θ between the Bloch vector and $|\mathrm{g}\rangle$ is always smaller than 5°. For the states described in Fig. 3, the angles are from left to right 15°, 3°, 13°, 4°, and 9°, due to less precise tune-up of the sequences for some of the states. The length of the Bloch vector is close to 0.8 in Fig. 4 and slightly larger in Fig. 3. This decrease in amplitude could be due to errors in the preparation sequence that leave the qubit and resonator somewhat entangled. However, we attribute the reduction in visibility mostly to decoherence: The preparation sequences for the states in Fig. 4 take approximately 200 ns, a time slightly longer than the Ramsey coherence time $T_2 = 150$ ns of the qubit. This implies that when the qubit is brought into an equal superposition of $|\mathrm{g}\rangle$ and $|\mathrm{e}\rangle$ and left there for a time of 200 ns (worst case), the length of the Bloch vector would be reduced to 0.25. The qubit decoherence is actually less than this because the state is typically not in an equal

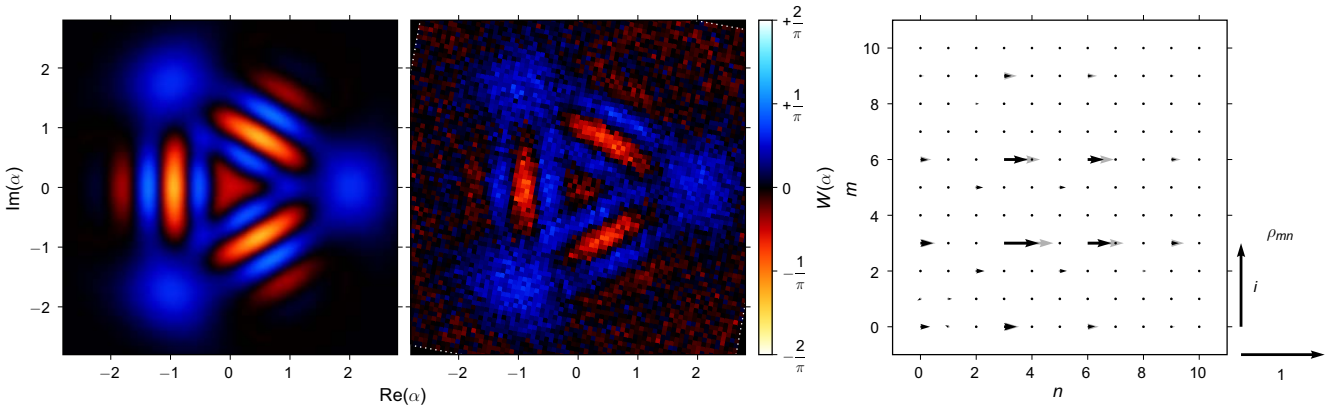

Figure S1 | Wigner tomography of a "Voodoo cat" state. Left panel is theory, middle panel is experiment, and right panel is the comparison of the density matrices, as in the main article. This "Voodoo cat" state is an equal superposition of coherent states $|\alpha = 2\rangle$ ("alive"), $|\alpha = 2e^{2\pi i/3}\rangle$ ("dead") and $|\alpha = 2e^{4\pi i/3}\rangle$ ("zombie"). The state can be expanded in the Fock basis as $\sum_{n=0,3,6,9\ldots} (2^n/\sqrt{n!})|n\rangle$. For the experimental realisation we have truncated the expansion at $n = 9$. Theory and experiment match well (fidelity $F = 0.83$), indicating that states up to nine photons can be created accurately.

superposition of $|\mathrm{g}\rangle$ and $|\mathrm{e}\rangle$. In addition, the qubit frequency is partially stabilised when it is interacting with the resonator.

Because the qubit is only weakly entangled with the resonator, we can read out the resonator state with the qubit. In doing so we must account for a reduction in the readout visibility due to the reduced length of the qubit Bloch vector after the preparation sequence.

We perform photon number readout on the resonator by bringing the qubit on resonance ($\Delta = 0$) for a variable time and then measuring its excited state probability P_e. With the qubit on resonance and no drive signals, all terms in Eq. (1) vanish except for the interaction. If the qubit-resonator state at the beginning of this resonant interaction is described by the system density matrix $\tilde{\rho}$, the probability to measure the qubit in the excited state after time τ is

$$P_\mathrm{e}(\tau) = \frac{1}{2}\left(1 - \tilde{\rho}_{(\mathrm{g},0),(\mathrm{g},0)} - \sum_{n=1}^{\infty}\left(\left(\tilde{\rho}_{(\mathrm{g},n),(\mathrm{g},n)} - \tilde{\rho}_{(\mathrm{e},n-1),(\mathrm{e},n-1)}\right)\cos(\sqrt{n}\Omega\tau) + 2\mathrm{Im}(\tilde{\rho}_{(\mathrm{e},n-1),(\mathrm{g},n)})\sin(\sqrt{n}\Omega\tau)\right)\right). \quad (9)$$

The qubit is mostly disentangled from the resonator and nearly in the ground state, and thus we can neglect the last two terms of Eq. (9), simplifying this relation to

$$P_\mathrm{e}(\tau) \approx \frac{1}{2}\left(1 - P_\mathrm{g}\sum_{n=0}^{\infty} P_n \cos(\sqrt{n}\Omega\tau)\right), \quad (10)$$

where P_g is the probability for the qubit to start in its ground state and $P_n = \rho_{nn}$ are the diagonal elements of the resonator density matrix. The probabilities P_n may now be extracted from the measured time evolution $P_\mathrm{e}(\tau)$ by performing a least-squares fit of the data with cosine oscillations at the various frequencies $\sqrt{n}\Omega$.

We measure the Rabi coupling frequencies $\sqrt{n}\Omega$ by driving the resonator with a coherent microwave pulse, generating a coherent state, then measuring $P_\mathrm{e}(\tau)$. Fourier transforms of $P_\mathrm{e}(\tau)$, taken for a range of drive amplitudes, give sharp peaks at frequencies $\sqrt{n}\Omega$ that are used for calibration.

With P_g and $\sqrt{n}\Omega$ already determined, calculating P_n from Eq. (10) becomes a *linear* least squares fit, which yields stable and robust results.

In our earlier experiment[8], decay of resonator states during measurement required the introduction of visibility factors. Because coherence times are longer here, visibility factors would be greater than 95 % and are not absolutely required to correct for the decay of the Fock states during measurement. Nevertheless, the precision of the photon number analysis was improved by including decoherence into the calculation of $P_\mathrm{e}(\tau)$. We numerically solve the Lindblad master equation[31] for the qubit coupled to Fock states, including the same Hamiltonian evolution as Eq. (1) but with the relaxation times $T_{1,\mathrm{r}} = 3.5\,\mu\mathrm{s}$ for the resonator and $T_{1,\mathrm{q}} = 650\,\mathrm{ns}$ for the

qubit and using the dephasing time $T_{\phi,\mathrm{q}} = 300\,\mathrm{ns}$ for the qubit (resonator dephasing is much slower than $3.5\,\mu\mathrm{s}$ and not included in the model). Note that we use a larger qubit dephasing time than measured for the qubit alone, which accounts for the stabilising effect of the resonator on the qubit. As we do not know of any theory precisely predicting this stabilising effect, the qubit dephasing parameter was adjusted to best match the observed time evolution.

Although we typically fit for photon numbers up to $n_{\mathrm{fit}} = 15$, the results are significant only up to $n_{\max} = 10$. We fit more photons than needed because the oscillations from P_n are not orthogonal, so P_n from the highest n absorbs some probability from non-fitted photon numbers.

4. PULSE CALIBRATION

As illustrated in Table 1 in the main article, the intermediate states during state generation are quite complex. This complexity discourages the measurement of intermediate states to tune the sequences. Instead, we carefully calibrate the fundamental operations, the single qubit Rabi pulse, the qubit-resonator photon swap, and the qubit-resonator phase accumulation, thus obviating the need to tune up individual sequences. The calibrations of the microwave electronics described here are fully automated. The qubit calibrations are semi-automated and require standard adjustments of the bias and read-out, which are not detailed here.

4.1. Calibration of the microwave circuitry

We control the qubit using flux bias and microwave pulses. The flux bias is applied via two separate signal lines, one heavily low-pass filtered but weakly attenuated allowing large flux bias excursions at low speed, the other unfiltered but heavily attenuated allowing small excursions at high rates. The lines are combined in the experimental cryostat at a custom inductive bias-tee just outside of the sample mount. This summed current inductively couples magnetic flux to the qubit. The microwave line has two broadband (20 GHz) 20 dB attenuators placed at 4 K and the mixing chamber and capacitively couples current to the qubit.

4.1.1. Slow flux bias

The slow flux-bias waveform is generated by a custom low-speed and high-accuracy digital to analog converter (DAC) based on the MAX542[32]. For low noise performance, its digital inputs and clock are held constant during qubit operation.

4.1.2. Fast flux bias

The fast flux-bias waveform is generated by custom DAC electronics[32] based on the AD9736, which gives 14 bit resolution at a 1 GHz sampling rate. Its two differential outputs are sent through separate Gaussian low-pass filters[32] with a 3 dB roll-off frequency of 200 MHz, and then to a differential amplifier (THS4509) for low distortion amplification and conversion to a single-ended output. To correct for imperfections in this electronics chain, we first generate a step-edge output from the DAC and measure with a sampling oscilloscope the output waveform. Using de-convolution techniques, we then digitally correct any desired waveform with the measured response of the step-edge.

The 200 MHz low-pass filters considerably suppress signals close to the DAC Nyquist frequency of 500 MHz. The de-convolution correction compensates for this suppression and greatly amplifies signal components close to the Nyquist frequency, causing various artifacts. We add a software low-pass filter to prevent this amplification of high frequency components, as well as ringing due to a sharp cutoff at the Nyquist frequency. We found that a Gaussian low-pass filter with a 3 dB frequency of 150 MHz, worked well with our electronics chain.

This calibration from the sampling oscilloscope eliminates all distortions outside the cryostat. Wiring imperfections inside the cryostat may also be measured and corrected by using the qubit as a sampling oscilloscope. We use the flux-bias dependence of the qubit transition frequency to measure how the actual flux bias evolves in time: We first tune a 8 ns FWHM resonant microwave π-pulse in amplitude and frequency to yield a high fidelity $|\mathrm{g}\rangle \rightarrow |\mathrm{e}\rangle$ qubit transition (see below). We then add a $1\,\mu\mathrm{s}$ flux-bias pulse just before the microwave pulse. The flux waveform is much longer than the ~ 100 ns timescale over which imperfections are observed, so we only consider the second (falling) flank of the waveform. In the absence of imperfections, the flux bias following the test waveform will settle to its pre-waveform value, and the microwave swap pulse will be precisely resonant with the $|\mathrm{g}\rangle \rightarrow |\mathrm{e}\rangle$ transition. In actuality, we find that the qubit frequency is slightly de-tuned, so the π-pulse fidelity is reduced. We then add a flux bias offset to bring the qubit back on resonance and return the fidelity of the π-pulse to its original value. By scanning flux offset and timing, we can map out the response of the qubit to the flux bias step. We then correct for this response in the same way as for the response function measured with the oscilloscope. Because this method has only a limited time resolution due to the finite length of the microwave pulse, we correct for fast distortions outside the cryostat.

4.1.3. Microwave drive

For the microwave drive for qubit and resonator we use a single microwave source (Anritsu 68369A/NV), modulated by IQ mixers (Marki IQ0307LXP). The I and Q channels of each mixer are driven by two DAC outputs identical to the fast flux bias. The mixers generate single-sideband microwaves that can vary in frequency, phase, and amplitude. We phase-lock all five DAC channels to an external 10 MHz clock, and digital communication between the DACs ensures that the waveforms are synchronised with each other and the microwave source. We perform 3 types of calibrations for the microwave signals:

DAC zero adjustment ensures that the IQ mixer output can be turned off precisely, eliminating bleed-through of the carrier signal. In principle, a small magnitude of carrier leakage is not a problem because, as we use sideband mixing, the carrier frequency is typically not resonant with the qubit or resonator. However, we typically place the carrier frequency between qubit and resonator frequency. Since the qubit is swept through the carrier frequency each time it is tuned into resonance with the resonator, carrier leakage could slightly perturb the qubit state. To calibrate the I and Q DAC values needed to zero out the mixer, we measure the mixer output with a spectrum analyser in a very narrow frequency band around the carrier frequency. A simple search allows both I and Q to be zeroed: We first fix the Q channel DAC and measure the power for 3 different I DAC values, finding the minimum from a parabolic fit. We then fix this I value and measure the power for three Q values, finding the best Q value in the same way. This sequence is repeated over increasingly narrow ranges until the resolution of the DAC is reached. We typically find carrier on/off ratios of > 70 dB. We also find DAC values for zero are strongly dependent on carrier frequency.

Sideband mixing generates a shift $\Delta\omega$ in the carrier frequency ω by applying a signal of frequency $\Delta\omega$ to the I and Q ports of the mixer. A single sideband is generated when the signal to port Q is phase shifted by $\pi/2$ with respect to port I. IQ mixers are imperfect, and deviations exist in both the amplitude sensitivities and the relative phase, which gives rise to an opposite frequency sideband at $-\Delta\omega$. We cancel this undesired signal by adding to the digital I and Q waveforms a compensating signal of adjustable amplitude and phase at $-\Delta\omega$. To adjust this compensating signal, we measure the undesirable sideband signal with a spectrum analyser and adjust the real and imaginary part of the compensation to achieve an absolute minimum, with the same search pattern as for zeroing of the DACs. We find the compensation depends both on the carrier frequency ω and the sideband frequency $\Delta\omega$.

Deconvolution calibration is similar to that performed for the flux bias signal. Here, we measure the pulse response at microwave frequencies. After calibrating the DAC zero and sideband mixing, we apply a 1 ns impulse to port I and measure the output of the IQ mixer with a sampling oscilloscope. The impulse response is then obtained by numerically demodulating the carrier frequency. The same measurement is then repeated for port Q. As this calibration is slow, it is performed only for a single carrier frequency, typically 6 GHz. This simple calibration is sufficient because the microwave signals do not have stringent requirements on the pulse shape. We find precise calibration of the sideband mixing is of greater importance.

4.2. Qubit microwave pulses

When microwave pulses are used to generate qubit transitions $|g\rangle \leftrightarrow |e\rangle$, excitations to higher energy levels must be avoided, in particular the next higher eigenstate $|2\rangle$. The $|2\rangle \leftrightarrow |e\rangle$ transition frequency is typically 200 MHz lower than $|e\rangle \leftrightarrow |g\rangle$ due to the limited non-linearity of the phase qubit. Microwave pulses for $|g\rangle \leftrightarrow |e\rangle$ therefore need to have low spectral component at the $|e\rangle \leftrightarrow |2\rangle$ transition frequency, so the pulses must be sufficiently long and accurately shaped. We program the pulses to have Gaussian envelopes with 8 ns FWHM, which were measured to yield negligible population ($\lesssim 10^{-4}$) of the $|2\rangle$ state[33].

We calibrate single qubit Rabi pulses with the $|g\rangle \rightarrow |e\rangle$ transition, which corresponds to a rotation π on the Bloch sphere. For this calibration, we maximise the measured probability P_e by adjusting the amplitude and frequency of the microwaves, as described in a previous experiment[33] that obtained a gate fidelity of 98 %. For Bloch sphere rotations with smaller angles, we simply scale the pulse amplitude. Nonlinearities in the DAC and from the AC Stark effect generate errors of less than 2 % in the rotation angle.

4.3. On-resonance tuning

We typically de-tune the qubit by ≈ 500 MHz below the resonator frequency for a qubit-resonator coupling of $\Omega/2\pi \approx 20$ MHz. By operating below the resonator frequency, the qubit is not swept through this resonance when measured and higher level transitions of the qubit do not cross the resonator frequency. To calibrate the flux bias pulse that tunes the qubit into resonance with the resonator, we prepare the qubit in the $|e\rangle$ state using a microwave Rabi pulse (see above), apply a flux bias tuning pulse with a variable amplitude and duration, and then measure the excited state probability P_e. Close to resonance, a single photon is swapped between the qubit and resonator at the frequency

$$\Omega' = \sqrt{\Omega^2 + \Delta^2} \tag{11}$$

which equals the coupling strength Ω when the qubit and resonator are on resonance ($\Delta = 0$). The resonance condition is precisely measured by varying the tuning pulse amplitude and duration τ, mapping out P_e as shown in Fig. 2 of the article. We then Fourier transform $P_e(\tau)$ for different flux biases, and fit the maxima of the Fourier transform to Eq. (11) to find the flux bias amplitude that gives the minimum swap frequency. This fit is shown in Fig. 2d of the article.

4.4. Swap pulse calibration

With the magnitude of the flux bias pulse determined from the previous calibration step, we next precisely adjust the length of the swap pulse so that the photon is completely transferred from the qubit to the resonator. We optimise transfer by minimising the probability P_e of finding the qubit in its excited state after the transfer.

The shape of the rising and falling edges of the flux bias pulses is defined by the 150 MHz numerical Gaussian low-pass filter (see section 4.4.1), and is error-function shaped with a 10 % to 90 % rise time of 2.3 ns. The finite duration of the pulse rise and fall time, during which the qubit is approaching resonance while interacting with the resonator, limits the fidelity of the photon transfer. To compensate for this effect, we add a Gaussian-shaped overshoot to the beginning and end of the pulse, bringing the qubit frequency slightly past the resonator frequency. The Gaussian is centred at the step edge and its FWHM of 2.1 ns is also defined by the numerical low-pass filter. The pulse duration and overshoot height are adjusted alternatingly several times to reach the global minimum in P_e.

Once the transfer of the first photon is optimised, we repeat the procedure for the second photon: A microwave Rabi pulse is added immediately after the first swap pulse bringing the qubit into the $|e\rangle$ state, and then the swap pulse is optimised for minimum P_e. We typically repeat this optimisation procedure for up to six photons, which represents generation of Fock states in the resonator. The amplitude of the optimal overshoot only depends weakly on photon number. As calibration cannot depend on photon number for arbitrary state generation, we average the overshoot and apply this value for all the swap pulses. Using the average overshoot, we then repeat the calibration procedure for only the pulse duration, finding swap times for up to 15 photons.

We use these swap times to calibrate the swap operation for arbitrary state generation. Since the coupling strength scales as $\sqrt{n}$, where n is the photon number, the n-photon swap time will result in a swap angle of $\phi = \pi/\sqrt{n}$ when applied to the ground state of the resonator. Thus, when plotted versus $1/\sqrt{n}$, as in Fig. S2, all swap times should fall on a line, whose slope and intercept give the calibration for the swap operation.

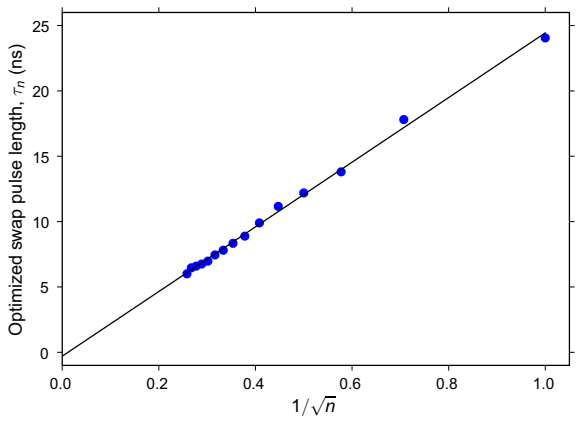

Figure S2 | Calibration of the photon swap operation from the measurement of optimum swap time versus $1/\sqrt{n}$. The optimum time for the n-photon swap pulse is measured by maximising state transfer to the resonator, resulting in the generation of Fock states. Because coupling strength scales as $\sqrt{n}$, the data should fall on a line. The slope and offset time of this line is used to calibrate the swap operation for arbitrary state generation.

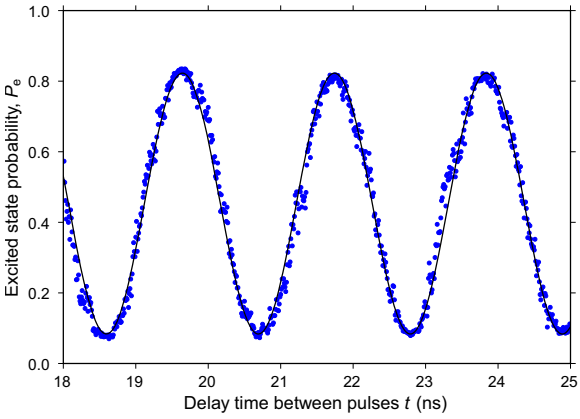

Figure S3 | Ramsey interferometry between qubit and resonator. The sequence consists of a qubit π pulse followed by two half-swaps separated by a variable delay time t, then measurement of the qubit state. Delay times t only need to be scanned around 20 ns, which are relevant for the arbitrary state pulse sequence.

4.5. Phase accumulation rate

When the qubit is de-tuned from the resonator, the $|e, n\rangle$ states accumulate phase with respect to the $|g, n+1\rangle$ states at a rate $\Delta_{\text{off}} = \omega_q - \omega_r$, roughly $-2\pi \times 500$ MHz. For generating states more complex than Fock states, this phase must be taken into account. To calibrate phase accumulation, Ramsey interferometry is used between the qubit and resonator: We first prepare the qubit in the $|e\rangle$ state with a swap pulse, and then perform a half-swap to the resonator. After a variable time t we perform a

second half-swap, and measure P_e as a function of t. As seen in Fig. S3, the probability oscillates sinusoidally at the phase accumulation rate. The two half-swaps add to a full swap, yielding a minimum P_e, when the delay time t yields a phase accumulation of a multiple of 2π. For phase accumulation of π, the second half-swap undoes the first half-swap, yielding a maximum value for P_e. The oscillation allows a precise calibration of phase accumulation when the qubit and resonator are de-tuned.

Note that the timing of the pulses in Fig. S3 require nearly continuous variation of t. The pulse edges can be adjusted for a time much less than the 1 ns DAC update time because the step edges are generated from several DAC points. As illustrated in Fig. S3, we can adjust and control the step edges in the $10 - 50$ ps range.

References

8. Hofheinz, M. *et al.* Generation of Fock states in a superconducting quantum circuit. *Nature* **454**, 310–314 (2008).
15. Steffen, M. *et al.* State tomography of capacitively shunted phase qubits with high fidelity. *Phys. Rev. Lett.* **97**, 050502 (2006).
24. Haroche, S. & Raimond, J.-M. *Exploring the Quantum — Atoms, Cavities and Photons* (Oxford, 2006).
28. Leibfried, D. *et al.* Experimental determination of the motional quantum state of a trapped atom. *Phys. Rev. Lett.* **77**, 4281–4285 (1996).
30. Lougovski, P. *et al.* Fresnel representation of the Wigner function: An operational approach. *Phys. Rev. Lett.* **91**, 010401 (2003).
31. Lindblad, G. On the generators of quantum dynamical semigroups. *Comm. Math. Phys.* **48**, 119–130 (1976).
32. For detailed information and schematics see `http://www.physics.ucsb.edu/~martinisgroup/electronics.shtml`.
33. Lucero, E. *et al.* High-fidelity gates in a single Josephson qubit. *Phys. Rev. Lett.* **100**, 247001 (2008).